A Nature Portfolio journal



https://doi.org/10.1038/s43246-025-00972-3

3D full-field lacunar morphology and deformation of calcified fibrocartilage in the loaded Achilles enthesis of a mouse

Check for updates

Atousa Moayedi ¹□, Katerina Karali¹, Markus Boese², Jovana Radulovic¹ & Gordon Blunn³

Enthesis calcified fibrocartilage (CFC) is a specialized structure anchoring tendon or ligament to bone and transmitting stresses from joint motion or muscle forces. Understanding the CFC 3D microstructure—mechanics relationship is key to explaining its mechanical behaviour, failure, and regeneration after injury. Such insights can guide biomaterial design and regenerative therapies. However, current methods cannot non-invasively measure localized mechanical behaviour within this anisotropic, heterogeneous insertion. In this research, full-field micromechanical structural analysis of a murine enthesis (n = 3) was conducted to understand the mechanics underlying its structural attributes using high-resolution in-situ micro-computed tomography with deep learning reconstruction and digital volume correlation. Our findings reveal that, depending on stress angle, the central region of the CFC lacunar morphology deforms more than other regions. We also identified that CFC microstructure organization and thickness strongly correlate with strain distribution at the interface, with regions of higher lacunar density experiencing greater deformation.

The linking of tendons and bones tissues within the musculoskeletal system, such as the Achilles tendon to calcaneal bone, where two materials with different Young's moduli¹⁻⁴ are involved, is facilitated through a fibrocartilaginous interface⁵⁻⁷, termed an indirect enthesis. The anisotropic interface^{6,8} plays a crucial role in dispersing the force from the tendon into the bone. While the stress transmitted from the muscle to the tendon is reduced by tendon's recoil effect⁹, the structural transition from the tendon to uncalcified (UFC) and calcified fibrocartilage (CFC) zones provide additional resilience against this force^{4,10}, distributing load and accommodating tissue deformation. The fibrocartilage zones contain a heterogeneous arrangement of collagen fibres, mineral deposits, and extracellular matrix components, all of which contribute to the gradual transfer of load^{5,11}. These regions have a progressive mineralization and stiffness⁶ towards bone¹², expressing different mechanical responses⁴ and modulating stress concentrations that arise due to the differences in material properties between the tendon and bone. Although a healthy enthesis with progressive structural features generates a transition in stress concentration¹³, it is suggested that additional factors such as bone islands and osteons form a network in CFC contributing to the interlocking of the cement line¹³. These hierarchical architectural arrangements form a trabecular structure that define the CFC strength, anisotropy, and thickness therefore playing a crucial role in the mechanical response^{11,13,14}. While CFC thickness extension is formed based on the physiological strength and loading of the tendon or ligament¹⁵, it is believed that the fibrochondrocyte lacunae within the CFC have a role in the mechanical response of the enthesis to load. Therefore, their morphology and distribution are important for the force transmission as they can modulate the strain distribution in this region¹⁶ establishing the lacunar network of scientific interest¹⁷.

Several studies have investigated the structural and mechanical behaviour of tendon-to-bone interface by identifying the strain and mechanical response at the insertion site^{4,6,18-24}. Histology is widely used for identifying tissue structures and it provides deep insights into morphology at the microscopic level²⁵. Confocal microscopy and scanning electron microscopy-based techniques are capable for nanoscale imaging. However, such methods limits observations to two-dimensional (2D) perspectives and the inability to detect localized deformation of the tissues under physiological load^{26,27}. Additionally, sample preparation in some techniques may affect the material properties impacting realistic mechanical behaviour. This limitation has restricted accurate three-dimensional (3D) quantification of enthesis structure, lacunar morphology, distribution and their response to load within the CFC region, which is significantly relevant to bone research²⁸, as alterations in lacunar morphology are frequently associated with disease states²⁷. Here, the hypothesis is that small alterations in the lacunar network could affect the force dissipation within and across the enthesis. However, the localized deformations of the CFC structure, and mechanical performance are still unknown and this limits the

¹School of Electrical and Mechanical Engineering, University of Portsmouth, Portsmouth, UK. ²Materials Science, Carl Zeiss Microscopy GmbH,
Oberkochen, Germany. ³School of Medicine, Pharmacy and Biomedical Sciences, University of Portsmouth, Portsmouth, UK. ⊠e-mail: amoayedi01@qub.ac.uk

understanding of the CFC function. The inability to analyse intact samples has hindered the understanding of the response of CFC structure to mechanical loading. The relationship between the microstructure of CFC and its localized deformation patterns remains an area requiring further investigation.

Micro computed tomography (micro-CT) is considered as a nondestructive technique, providing high spatial resolution, while offering optimal field-of-view^{29,30}. This technique combined with digital volume correlation (DVC)31, has enabled full-field and tissue-level strain measurements in biological tissues^{31–33}. However, to achieve a high-resolution fullfield imaging at the microscale level, the samples need to be scanned for several hours, which can affect tissue hydration and, consequently, mechanical properties. Herein, we present an approach to investigate the full-field microstructure of CFC, and fibrochondrocyte lacunar morphology of the murine Achilles tendon-to-calcaneus bone interface under localized tensile strain, using in-situ loading and high-resolution micro-CT combined with DVC and a deep learning reconstruction technique³⁴ that reduces scanning time to maintain tissue mechanics (Fig. 1). In this technique, the specimen undergoes no sample preparation, preserving the tissue's natural state during mechanical testing while capturing the microstructure across the entire interface. Moreover, image post-processing is critical for extracting reliable lacunar network from micro-CT datasets. The polychromatic nature of the X-ray beam introduces artifacts that must be minimized to ensure accurate analysis³⁵. One underexplored but critical step in improving segmentation accuracy across different samples is histogram matching before thresholding³⁶. This process aligns the tissue mineral density and grey level distributions of all samples to a standard reference. This is particularly important when studying lacunae under different experimental conditions, such as pre-load and load-induced displacement, where variability can arise from factors such as sample positioning after insitu micro-CT tensile loading affecting the voxel intensities.

Results

3D microstructure of calcaneus calcified fibrocartilage (CFC)

Figure 2 shows the three-dimensional high-resolution microstructure of calcaneus tuberosity of the murine Achilles insertion including the fibrochondrocyte lacunae in the calcified fibrocartilage zone, the cortical shell thickness, and the trabecular microstructure of the CFC captured using micro-CT with the X-ray source and the detector positioned at optimal distances for an isotropic voxel size of 1.33 microns. Following CT reconstruction using the Feldkamp-Davis-Kress (FDK) algorithm³⁷, the dataset was repositioned to align the cross-sectional planes with the bodies anatomical planes for precise structural analysis. Images represent the CFC curvature that spans up to $911.17 \pm 10.79 \mu m$ (mean \pm SD) along the mediolateral axis. It extends cranially up to $312.34 \pm 20.93 \,\mu m$ (mean \pm SD) at the central region. The tuberosity reaches a peak elevation of 182.32 ± 22.15 µm (mean \pm SD) along its anteroposterior axis, predominantly cantered within its structure. At the external posterior region of the protrusion, the CFC is encased by the cortical shell with thickness of $21.58 \pm 3.04 \, \mu m$ (mean \pm SD). Beyond this boundary, the CFC structure starts anteriorly, and it persists along the inward extension of the sloping surface. The CFC local thickness distribution pattern is analysed in three planes corresponding to the sagittal, transverse, and coronal orientations at the Achilles to calcaneus insertion.

The wall spacing at the CFC within the lacunar network is $12\pm1~\mu m$ (mean \pm SD) [min: 5 μm , max: $22~\mu m$]. The images show that the overall CFC thickness within sagittal planes is slightly different between the central (107 \pm 9.22 μm) and peripheral (91.86 \pm 6.92 μm) regions (mean \pm SD). The posterior CFC thickness reaches up to 263.08 \pm 16.65 μm and decreases anteriorly to an expanded CFC thickness of 65 \pm 10.81 μm (mean \pm SD). The overall CFC thickness distribution is 84.34 \pm 6.98 μm (mean \pm SD) in transverse planes, decreasing proximally and distally (Supplementary Fig. 2, 3, and 4, Supplementary Movie 1). The lacunar structures in the CFC are arranged in nearly parallel, elongated strands that curve towards the central protrusion. Each lacuna has a volume ranging from 50 to 1000 μm^3 , with the

larger lacunae mostly located in the central region. The larger lacunae have rod-like shape and are elongated, while the smaller lacunae are mostly plate-like and spherical and are spread between the large lacunae, as well as concentrated around them and are closer to the cortical shell. Based on micro-CT grey-levels, the mineral density between the lacunae within the CFC is lower in this region compared to the underlying bone and the cortical shell. The lacunar porosity within the CFC protrusion is higher than in the periphery. In the central region of the protrusion, the lacunar strands are longer, reaching an average length of $168\pm3.41~\mu m$ (mean \pm SD). The CFC is demarcated from the underlying bone by an irregular, serrated, and undulating cement line.

Full-field micromechanics of the enthesis CFC

To investigate the strain concentration within the CFC of the murine Achilles to bone insertion, we developed an in-situ micro-CT uniaxial tensile testing methodology, incorporating an advanced deep-learning reconstruction algorithm. This approach facilitated the rapid acquisition of high-resolution micro-CT datasets captured in 52 minutes by reconstruction (DR) through the training of the datasets using neural network models (Supplementary Note 1, Supplementary Figs. 5 and 6) compared to the standard micro-CT reconstruction (FDK). This non-destructive technique effectively preserved the tissues natural state and significantly increased the resolution of anatomical features by enhancing the signal-to-noise ratio (SNR) by a factor of two for low-projection number datasets and up to a factor of five for higher projection numbers (Supplementary Fig. 7) with minimal impact on the DVC error uncertainties, quantified at an average of 507 ± 226 (mean \pm SD) micro-strain difference at smaller sub-volumes between FDK and DR reconstructed images taken at certain projection number (Supplementary Figs. 8 and 9). Contrast-to-noise ratio (CNR) was optimized by scaling histograms using a bone-like phantom reference. This allowed us to capture images with enhanced contrast and an improved signal-to-noise ratio within a significantly shorter time interval that would have been greatly extended had the deep learning algorithm not been used and the use of this prevented damage to the tissue through exposure to high radiation dose.

To quantitatively assess the response of CFC to uniaxial tensile loading and the corresponding strain distribution at a micrometre level, datasets 38,39 (Supplementary Movie 2 and 3) were analysed using DVC. This analytical framework yielded full-field displacement maps depicted as a vector field, effectively tracking the local changes between the pre-load volumetric image f(x) and the load-induced displacement image g(x+u). The correlation was achieved by using a large sub-volume FFT step to create an initial predictor displacement field for subsequent DC iterations through a multi-step cross correlation of progressively refined sub-volumes ranging from 22 to 52 voxels. Mathematically expressed as $C(u) = \sum_{x \in \Omega} [f(x) - g(x+u)]^{240}$ and the maps are presented in Fig. 3.

The vector field analysis under uniaxial tensile loading highlights a clear directional displacement pattern, with vector arrows indicating material movement posteriorly within the sagittal plane in the central region of the sample. The magnitude of these arrows is greater in the central area, suggesting a higher degree of displacement compared to the periphery, where the vectors are shorter, reflecting reduced deformation, which appears to be more structurally stable due to the presence of the cortical shell. This directional flow of the vectors showed that the wall spacing of CFC contracts with respect to the coronal axis under 4.5 N tension. The fullfield 3D strain quantities were extracted based on the post-processed vector field as illustrated in Fig. 3. The colour map represents the intensity of the strain at each voxel. The strain maps revealed that high-intensity areas of maximum normal strain (ϵ), reaching up to 0.7%, were most prevalent within the central region and inward protrusion of the CFC, adjacent to the columnar organization of the fibrochondrocyte lacunae, indicative of significant tensile deformation localized in this area. The maximum normal strain intensity decreased gradually towards the periphery (0.37%), and was close to zero within the cortical shell (Supplementary Movie 4). The strain level decreases anteriorly toward the underlying bone, attributable to the

CFC mineralization gradient⁶. The minimum normal strain reached a minimum intensity of -0.9%, reflecting regions under compressive stress. contributing to the overall mechanical stability of the CFC. Shear strain analysis further elucidated the complex mechanical environment within the CFC, with values peaking at 0.8%. The tensile strain generated in tendons is converted in part, to shear strains as a consequence of the complex morphology of the CFC lacunae and this means the CFC can accommodate multi-directional forces. The Poisson's ratio, based on the transverse strain response to axial loading, varied between -0.4 and 0.5 across the sample divided to voxels of 22 resulting in 29.3 µm intervals. In the protrusion and central regions, Poisson's ratio reached a peak of -0.4, indicating where lateral expansion occurs under axial strain which aligns with elastic behaviour in biological tissues, and auxetic material under load⁴¹⁻⁴³. Below the protrusion of the calcaneus, where the tissue is less porous and is adjacent to the underlying bone the Poisson's ratio ranged from 0.3 to 0.5. This observation is consistent with previous reports, particularly in regions of increased density and reduced porosity44.

CFC lacunar morphometric alteration under tensile loading

Analysis of the 3D population-based lacunar morphometric indices in unloaded state and under tensile loading was performed to quantitatively describe the CFC fibrochondrocyte lacunae distribution, and deformation morphology by processing the 3D datasets. In this research, for a precise thresholding, we first scale and match the pre-load and load-induced displacement tomograms histograms prior to applying thresholds using a bone-like phantom histogram intensity. To extract the lacunar network, the tomograms were binarized. To measure the binarization error 2 consecutive tomograms at the same load were acquired. The volume of randomly selected lacunae was calculated and compared to those of corresponding lacunae in the second tomogram. The volume and the standard error were calculated and varied by $\pm 10~\mu m$ or 1%. The opening morphological operation 45 was performed to separate connected binarized lacunae and enable their individual counting

and labelling. The small speckles in the background, and larger void structures in bone with the same grey intensity can be mistakenly identified as lacunae during segmentation due to artifacts in μ CT tomograms. The lacunae volume was restricted to 50-1000 μ m³, followed by morphological thresholds to exclude non-lacunar structures. The local lacunar morphometric analysis including lacunae volume (Lc. V), lacunae oblateness (Lc. Ob), stretch (Lc. St), and angle (Lc. Theta) unloaded and when loaded in tension (Supplementary Movie 5, 6, and 7) was measured and is presented in Fig. 4, Supplementary Fig. 11, and Supplementary Movie 8.

Analysis showed that the morphometric indices of fibrochondrocyte lacunae were different between pre-load and load-induced displacement. Before applying the tensile load, lacunae below 300 μm^3 were round with values between 0 to 0.5, and as the volume increased, the lacunae became more stretched with values between 0.5 to 1. Under load, larger lacunae were mostly between 0.4 to 0.6. The angle of lacunae with respect to the coronal plane had the highest frequency between 45 and 75 degrees, which increased during loading to 55 and 90 degrees. This indicates that the lacunae do not have a stable morphology under mechanical load (Supplementary Movie 9, 10, 11 and 12).

CFC full-field micromechanics and microstructure correlation

The CFC microstructure, including strain patterns and morphological features such as lacunae morphometry and CFC thickness, was analysed at high spatial resolution. DVC results from applied tensile loading revealed localized tissue deformation in the enthesis CFC, which was compared with high-resolution micro-CT tomograms to correlate the CFC trabecular structure, strain patterns, and morphometric indices. The strain pattern showed a strong positive correlation with lacunae number, volume, and shape decreasing towards the deeper zones of calcified fibrocartilage. We observed that the central region, which contains clustered large elongated lacunae, is more susceptible to deformation and exhibits the highest tensile strain, while the cortical shell layer remains

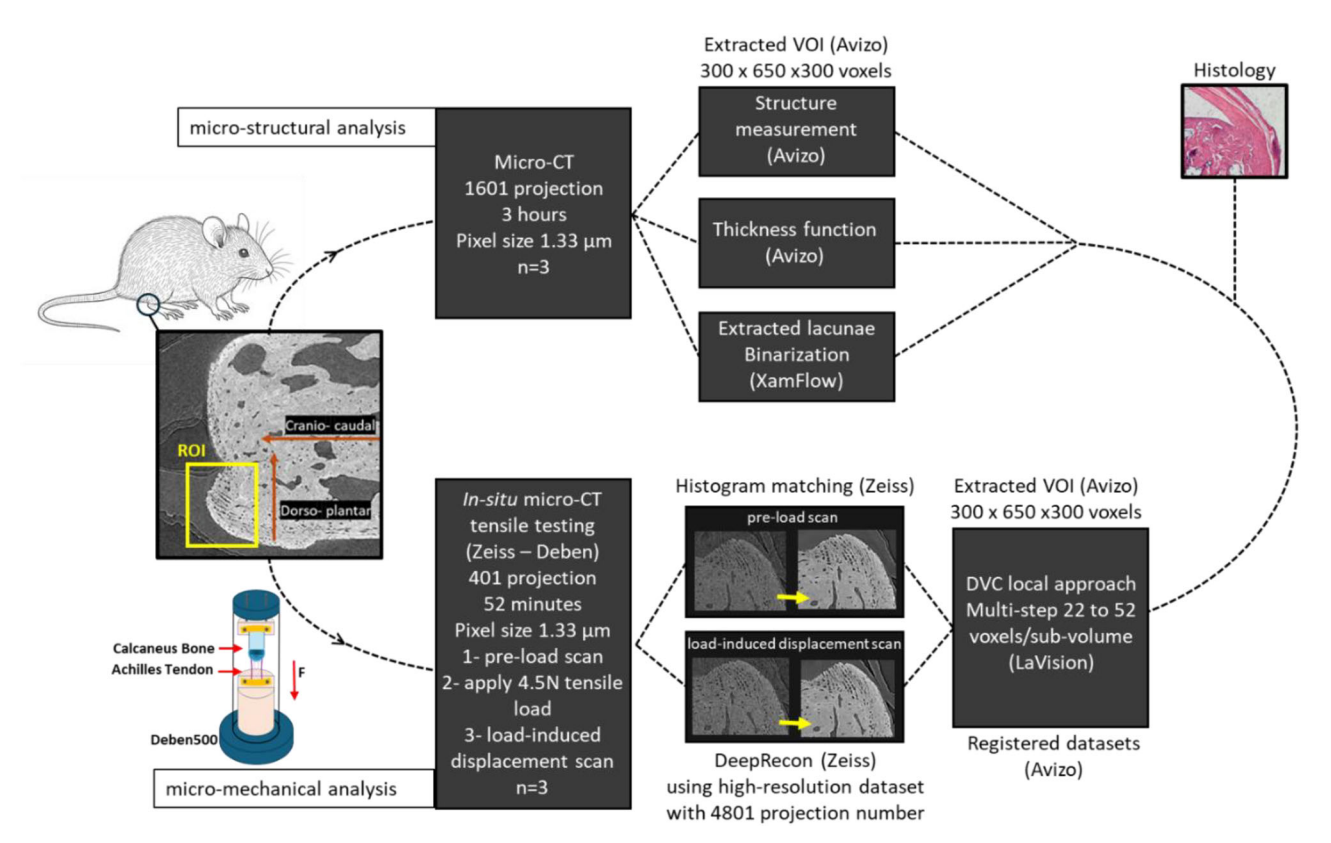


Fig. 1 | Workflow for high-resolution micro-CT imaging and in-situ tensile testing. Experimental setup highlighting the region of interest (ROI) at the tendon-to-bone insertion (Supplementary Fig. 1).

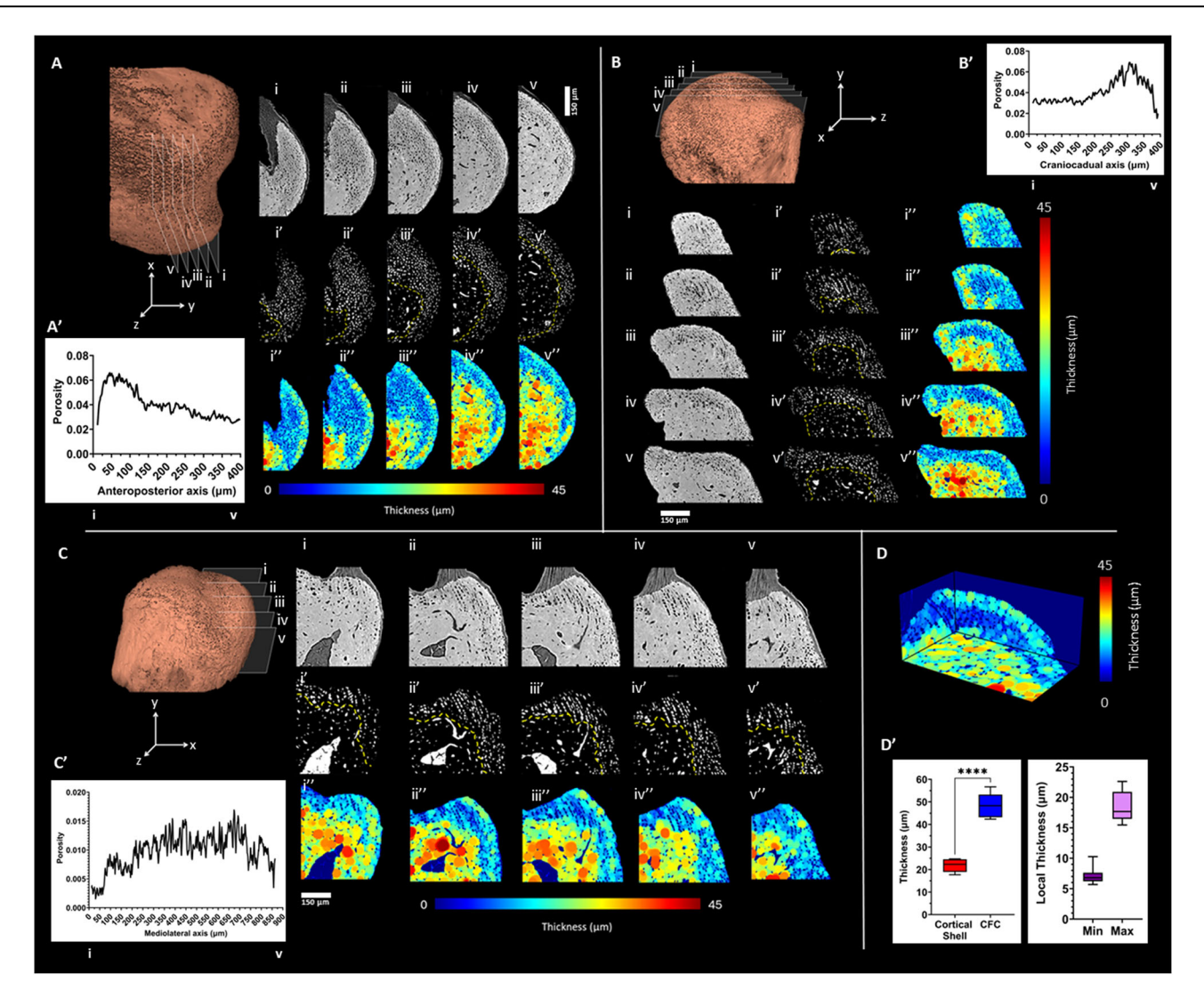


Fig. 2 | Calcaneus calcified fibrocartilage microanatomy. A Three-dimensional view of calcaneal tuberosity distal portion in medial position, (i–v) the planes mark the coronal slices (300 \times 650~ pixel size 1.3) at the 80–20% interval of the CFC passing through the ventral side of the tuberosity based on micro-CT datasets. (i'-v') corresponding binarized images representing lacunae distribution. (i"-v") trabecular thickness for selected micro-CT slice sections. The chromatic scale corresponds to thickness map, from relatively thin (blue) to relatively thick (red). B proximal cross sections, and (C) sagittal planes. D The local thickness distribution map for each plane in the CFC. A'-C' show the lacunar porosity distribution across the anteroposterior, craniocaudal, and mediolateral axes, respectively. The anteroposterior

axis shows an increase in porosity towards the tendon-calcaneus interface, with a decrease towards the underlying bone. Along the craniocaudal axis, porosity is higher near the CFC protrusion and lower at the cortical shell. The porosity profile along the mediolateral axis exhibits a higher peak at the centre, indicating increased porosity in this region. **D'** Box-and-whisker plots showing the thickness (in micrometres) of the cortical shell (red) and CFC (blue) on the left, and the local thickness at the minimum (Min) and maximum (Max) wall spacing on the right. On both plots, the boxes represent the interquartile range (min to max), with the horizontal bar indicating the median. ****P < 0.0001, showing a significantly greater thickness in the CFC compared to the cortical shell (error bar: 150 µm).

structurally intact. The central region of the protrusion has the lowest wall spacing, despite having the highest CFC thickness.

Scatter plots in Fig. 5 indicate that the highest maximum normal strain occurs in elongated columnar fibrocartilage lacunae within the central region, with a volume of $1000~\mu m^3$. Smaller lacunae (below $400~\mu m^3$) experience lower strain levels, reaching up to 0.3%. The relationship between strain patterns and fibrocartilage lacunae morphology was further demonstrated through morphological analysis of imaging data. The correlated data obtained from this non-invasive technique indicate that this protocol effectively explore microstructural evolution at the soft-to-hard tissue interface, correlating structural features with strain maps derived from DVC under physiological loading conditions. While this approach can extract the micromechanics of the material, it also enables precise identification of vulnerable regions within the tissue where the structure is more susceptible to fracture.

Discussion

The enthesis, where tendon fibres unravel and transition into the bone, forms a unique structure that accommodates a wide range of mechanical loads. This transition zone is characterized by a gradual change in material properties and a networked structure that likely contributes to the dissipation of mechanical stresses^{46,47}. The dissipation of energy at soft to hard tissues is influenced by multiple mechanisms including elastic deformation, molecular slippage, interactions of mineral content and collagen, and microstructural rearrangements^{48,49}. In this research, we demonstrated a direct correlation between the full-field local microstructural organization and mechanical behaviour of calcified fibrocartilage at the Achilles tendon-to-calcaneus interface under in-situ uniaxial tensile loading. Previous studies have made important advances in characterizing either the three-dimensional microarchitecture of the Achilles enthesis⁵⁰, and in capturing local deformation patterns within the region⁵¹, and microstructure and

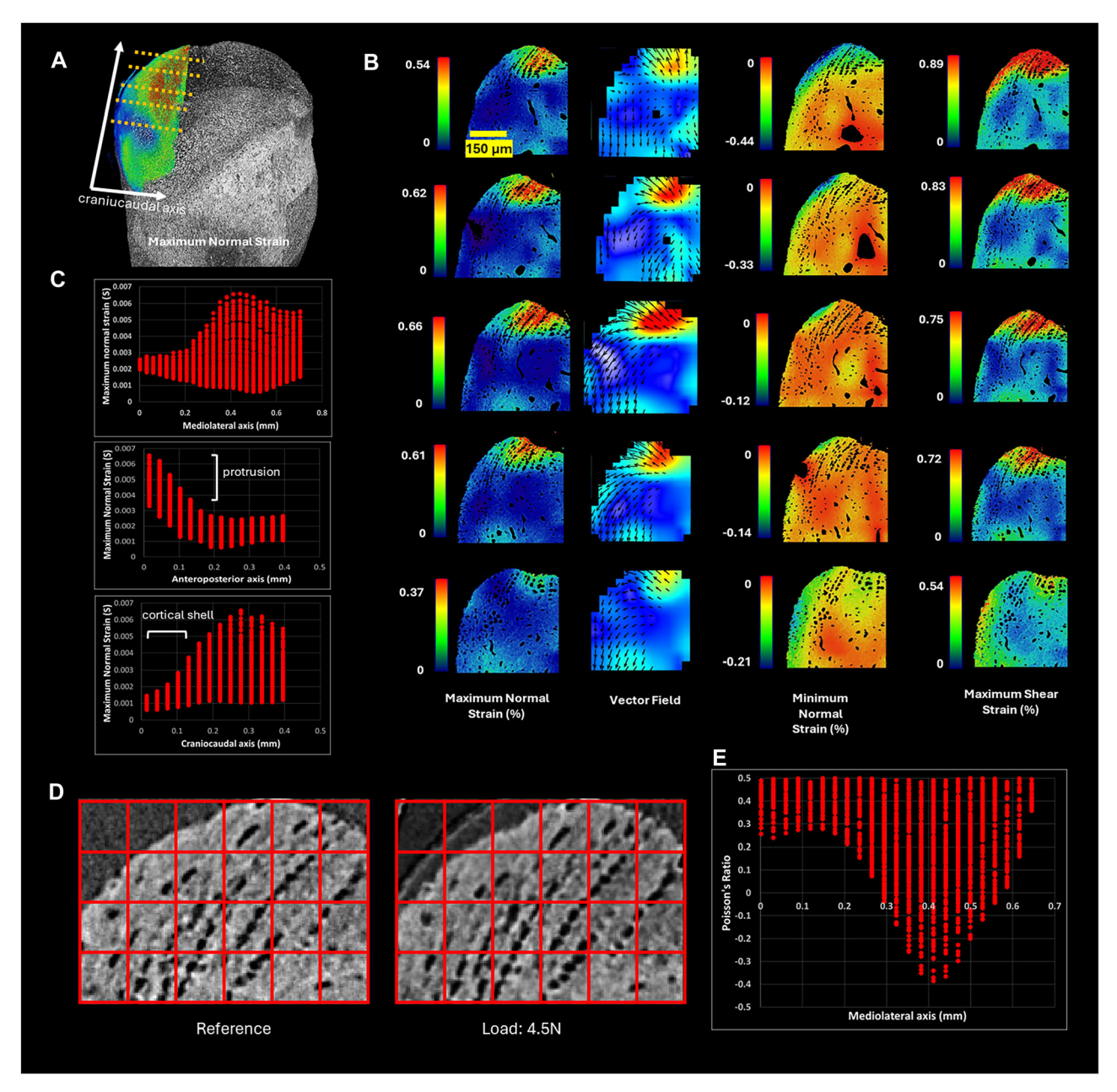


Fig. 3 | 3D strain mapping of calcified fibrocartilage. A 3D rendering of an 8-month-old mouse calcaneus loading (loaded specimen, 4.5 N tension) with the maximum normal strain map overlaid (data shown is for Sample No. 1; n=3, supplementary Fig. 10). The dotted yellow lines indicate the locations of the slices that are shown in the (B) respectively in the same order (error bar: $50 \mu m$). B Strain maps and vector fields analysis of CFC along the mediolateral axis. Panel (i) shows the maximum normal strain map for 5 cross-sections along the mediolateral axis, at 10-90% of CFC length (with 20% intervals), top to bottom, representing both ends of the axis. The colour map indicates the intensity of strain, with red showing the highest level of maximum normal strain. Panel (ii) presents the corresponding vector field with arrows representing the direction and magnitude of displacement and red colour shows the areas with higher deformation. Panel (iii) shows the minimum normal strain, and panel (iv) illustrates the maximum shear strain across

the slices, with red regions indicating areas of significant lateral deformation (error bar: $150\,\mu m$). C The plots show the distribution of maximum normal strain along different anatomical axes in the CFC. The top plot shows the strain along the mediolateral axis, it increases with distance, peaking at the central region of CFC. The middle shows the anteroposterior axis with a marked strain peak in the protrusion region. The bottom plot shows the craniocaudal axis, where strain decreases towards the cortical shell. D The left image shows a portion of CFC cross-section morphology before load, and the right image shows the same region under a 4.5 N load. The red grid overlay in both images represent the DVC voxels, with each grid square 29.3 μ m. The deformation in the tissue is aligned with the vector field direction. E Poisson's ratio distribution across the mediolateral axis of CFC showing the regional differences in the tissue's elastic behaviour.

micromechanics of enthesis including thin layers of CFC 4 . However, these studies have not simultaneously linked 3D microstructural features with corresponding mechanical responses at the micro-level within the CFC. By integrating the advanced high-resolution micro-CT imaging (voxel size 1.33 μ m) and DVC we quantified the localized strain and deformation and correlated these to lacunar morphology, organization, and alteration. In

addition to previous research on enthesis^{4,6,19}, this study provides a cross-correlation analysis of how hierarchical microstructural features modulate strain and highlights the lacunar deformation and morphological changes occurring as the CFC adapts to mechanical stress.

This study was performed on untreated specimens eliminating any potential effect on the material and mechanical properties across the

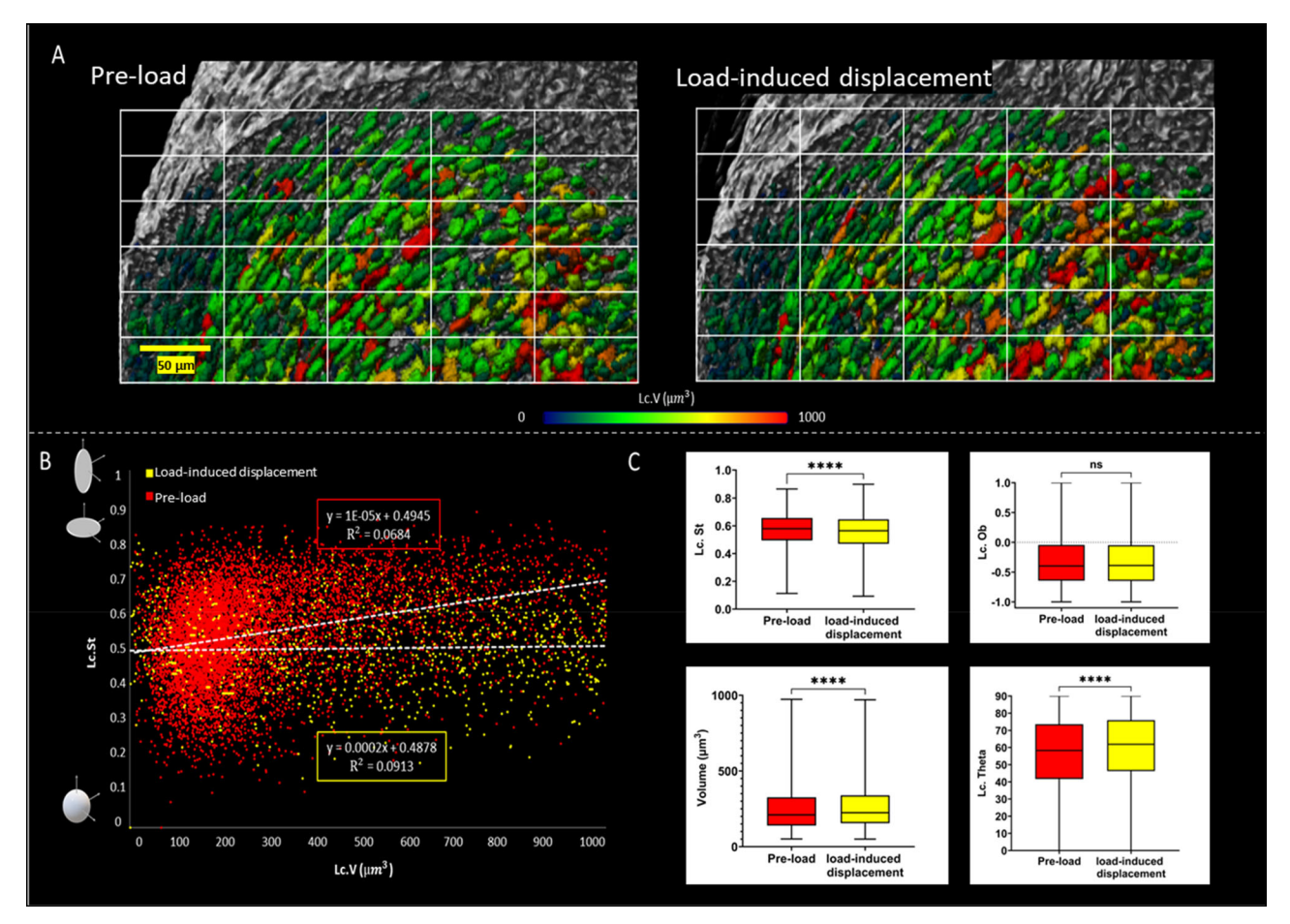


Fig. 4 | 3D morphometric analysis of calcified fibrocartilage lacunae. A 3D renderings of the segmented calcified fibrochondrocyte lacunae morphology under preload and load-induced displacement conditions. The colour map represents lacunae volume, ranging from 0 (blue) to $1000~\mu m^3$ (red). B The lacunae stretch (Lc. St) as a function of lacunar volume (Lc.V) before and after tensile load. C The four box plots show the distribution of top-left: Lc. St, top-right: Lc. Ob, bottom left: Lc. V, bottom right: Lc. Theta under pre-load (red) and load-induced displacement (yellow)

conditions. The boxes represent the interquartile range, with the median indicated by the horizontal line within each box. The whiskers extend to the minimum and maximum values, excluding outliers. A significant difference between the pre-load and load-induced displacement conditions is denoted by the asterisks (p < 0.0001). No significant difference in lacunae oblateness (ns, not significant), as indicated by the absence of asterisks.

experimental procedure, producing realistic mechanical behaviour of the CFC. The methodology preserves the inherent mechanical behaviour of the tissue, offering an accurate representation of the tissue physiological properties. The use of Deep learning-based reconstruction, provides an advantage by enabling high-quality imaging with a reduced number of projections and improves the DVC calculations by increasing the correlation value. This approach minimizes the need for long acquisition times, which can otherwise lead to sample dehydration, radiation damage and potential alterations in the tissue's mechanical properties.

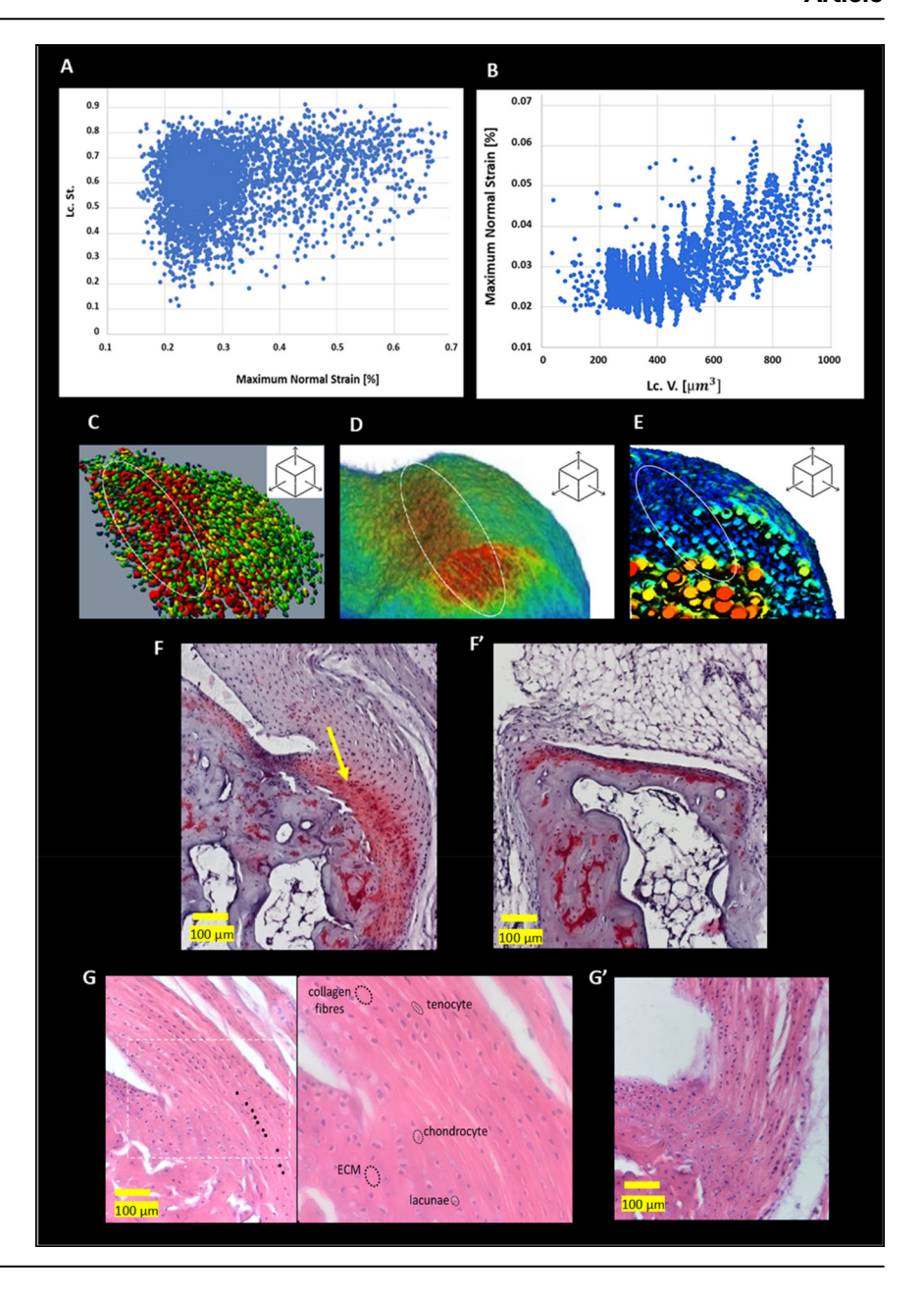
At a micro-level, we identified the areas undergoing higher strain where the lacunar network has a specific organization and experiences morphology alteration. Our findings reveal that depending on the angle of the applied stress, the central region of the CFC lacunar morphology deforms more than other regions. Furthermore, we identified that the CFC microstructural organization and thickness have a strong positive correlation with the strain distribution at the interface. Regions with higher lacunar porosity were found to experience greater deformation, suggesting that the local microstructure plays a crucial role in modulating the mechanical response of the CFC.

Our findings confirm the hypothesis that the CFC structure, lacunae morphometry and their alteration under load defines the anisotropy and the local mechanical properties of the CFC enthesis. By observing the localized strain concentration, we suggest that the CFC structure plays a critical role in accommodating and distributing mechanical loads, preventing excessive

strain in adjacent tissues. CFC possesses a highly specialized structure¹¹. The organized and elongated lacunar strands in the protrusion, in central regions and concentrated close to tidemark, form a more porous region in comparison to periphery. Moreover, there are lower CFC thickness in central areas. These characteristics combined with the mineral content and molecular composition^{4,6,11}, act as a stress concentrator, resulting in a heterogeneous mechanical response in this region. Larger lacunae exhibit a more oblate shape and are more prone to deformation under tensile loading, transitioning to a more spherical shape. The structural and morphological alterations may contribute to our understanding of previous research that presents the strong and stable anchorage at the interface, which aids musculoskeletal movement with appropriate integrity⁵. Moreover, the canalicular network in the bone underlying the CFC may be affected by lacunar elongation and morphological alterations, which can substantially influence the organization of the ECM^{52,53}.

Previous research has reported a general decrease in strain from tendon and ligament to bone attributed to mineralization gradient ^{4,23}, however, the local strain distribution across the CFC itself was unknown. The 3D full-field strain map at CFC exhibited a positive correlation with the 3D lacunae volume analysis. The strain response was nonlinear, with certain regions at the calcaneal apophysis showing higher strain levels (2-fold) where the lacunae columnar structure also had a larger volume creating expanded CFC thickness with the lower wall spacing compared to the bone. Therefore, it could be speculated that modification in structure under load, may

Fig. 5 | Correlation of calcified fibrocartilage lacunae morphometry with strain and histological features. A Scatterplots show linear correlations between average local volumetric strains and lacunar network volume and (B) lacunae stretch. C 3D representation of the lacunar network, with a colormap corresponding to lacunae volume (ranging from red, representing 1000 µm3, to blue, representing 50 μm3). D Maximum normal strain map (colormap indicating strain levels, with red showing the highest global strain level of 1). E 3D CFC thickness map (colormap illustrating thickness, from blue for the lowest to red for the highest values). F Safranin-O stained histological image of the enthesis at central region, highlighting a thicker layer of proteoglycan within the fibrocartilage and the tidemark (yellow arrow) separating fibrocartilage layers, and (F') Safranin-O staining at the periphery shows a thinner proteoglycan-rich layer and less fibrocartilage tissue adjacent to the attachment. GH&E stained pre-load histological section at central region showing collagen fibres (yellow arrowhead), tenocytes (red arrowhead), extracellular matrix (ECM, white arrowhead), lacunae (dotted black circles), and chondrocytes (black arrowhead). The small dots represent the count of chondrocytes within a lacunar strand in the calcified fibrocartilage. Fibrochondrocytes mostly towards bone and stretched toward tendon. G' load-induced displacement histological section at central CFC (error bar: 50 µm).



strengthen CFC in the force direction^{52,54}. The central strain gradually decreased towards the cortical shell, where the lacunae volume was noticeably smaller, confirming that the larger lacunae volume of fibrochondrocytes dissipates stress by increasing elasticity⁵⁵. Regions of high strain in the protrusion exhibited negative Poisson's ratio values, indicating a unique mechanical behaviour characterized by higher lateral expansion under axial load. This was further validated by lacunar analysis, which showed that lacunae become more rounded after loading, outlining their role in accommodating strain. Despite the lateral expansion, the CFC wall spacing contracts under uniaxial loading. This suggests that fibres extending from the lacunae towards the tendon contribute significantly to strain by expanding the lacunae under load. This finding highlights the importance of lacunae microstructural heterogeneity in modulating mechanical behaviour at the tissue level. Our observations of strain in the central region are consistent with previous research⁴ showing that the enthesis is designed to minimize stress concentrations, particularly at the tendon-bone interface, by distributing forces over a broader attachment area. The ability of this region to undergo controlled deformation may also contribute to its toughness²⁰, as suggested by the strain of accommodation observed in larger, and more oblate lacunae. The ability of the enthesis to modulate force transmission through both structural and material adaptations underscores its role in accommodating complex, multidirectional loads during movement.

While this study provides valuable insights into the microstructural mechanics of the enthesis, several limitations must be acknowledged. This study was conducted on a limited sample size (n=3). The primary aim of this work was to demonstrate the feasibility and utility of combining high-resolution micro-CT, deep learning reconstruction, and DVC for non-destructive, full-field mechanical and structural analysis. Future studies with larger sample sizes across different developmental stages are needed to extend these findings and further validate the changes induced by loading on the CFC microarchitecture. Further investigation should be conducted on lacunar deformation patterns across different age groups and species at different applied loads and angles. Additionally, while we focused on the mechanical and structural properties of the enthesis CFC, future research can incorporate molecular analyses in pre-load and load-induced displacement states, particularly investigating the full-field role of proteoglycans and collagen

modifications, which have been shown^{4,56,57} to influence tissue mechanics and fibre sliding behaviour.

We recognize that time-dependent strain may occur under constant load and displacement due to tissue viscoelasticity. To minimize its influence, scanning was initiated 15 min after reaching the target load to allow initial strain relaxation. In addition, we did not perform a post-unloading scan to confirm full recovery of the tissue deformation that would verify the loading remained within the elastic range. Although the applied load was within the linear region based on preliminary tensile-to-failure tests, future studies could include scanning to directly confirm elastic deformation and rule out any minor irreversible structural changes.

Our findings have important implications for understanding the broader principles of tendon-bone attachment mechanics and could provide valuable information for the development of biomimetic materials aimed at repairing or replicating the functionality of soft-hard tissue interfaces.

Methods

Sample preparation

For microstructural analysis, Achilles tendon attached to the calcaneus (n = 3) were dissected from euthanized 8 months old wild-type male murine (bred in-house) from, University of Portsmouth. Ethical approval was received from the School of Electrical and Mechanical Engineering, University of Portsmouth, under ethics number TETHIC-2022-104588. All methods were carried out in accordance with relevant guidelines and regulations and are reported in accordance with ARRIVE guidelines. Specimens were frozen at -20 C until used. While this study did not directly assess frost damage, previous research has shown that freezing tendon tissue at -20 °C does not significantly alter its microstructure or mechanical properties⁵⁸. Skin, tibia, and connective tissues around the Achilles tendon were removed under a dissecting microscope (Vision Engineering, UK) to ensure the tendon was fully intact. For micromechanical tensile testing, samples (n = 3) were cut into 20 mm segments and mounted onto the CT500 tensile testing stage (Deben, UK). The muscle-tendon junction (MTJ) was clamped to the mobile jaw and the calcaneus bone to the fixed jaw. Cyanoacrylate adhesive was used to secure sandpaper to each sample end to improve grip. The tendon's tensile axis was aligned with the calcaneus axis, and the MTJ was additionally glued to prevent rupture during loading⁵⁹.

High-resolution micro-CT data acquisition

The inner structure of the CFC was captured with ZEISS Xradia Versa 610 (Carl Zeiss Microscopy, Germany). The scans were conducted at 4X optical magnification with 21 mm distance between source and specimen and 85 mm distance between specimen and detector, achieving 1.33 μm isotropic voxel resolution, and a field of view 1400 $\mu m \times 1400$ μm to cover the whole murine calcaneal CFC. The X-ray tube voltage was 60 kV, and the power was 6 W. For each specimen, 1601 two-dimensional projections were acquired at 5-s intervals over a full 360° rotation and a total scan duration of 3 h. The 5-second exposure time per projection was selected to optimise the signal-to-noise ratio while accounting for the thickness and density of the murine calcaneal bone tissue 60 . CT reconstructions were performed using the FDK algorithm.

In-situ high-resolution micro-CT tensile testing

For mechanical testing, where dehydration was a concern, ZEISS ART 3.0 DeepRecon Pro (Carl Zeiss Microscopy, Germany) was utilized to enhance the signal-to-noise ratio in the datasets (Supplementary Note 1 and 2, Supplementary Figs. 5, 6, and 7). This tool enables the training of low-projection scans against high-projection scans to improve feature contrast and reduce scanning time. An initial scan comprising 4801 projections was imported, while subsequent scans (pre-load and load-induced displacement) were reduced to 401 projections. The datasets were trained on high-projection dataset acquired from the mouse Achilles and calcaneus sample, ensuring that structural features used for training were anatomically and

morphologically consistent with those used in low-projection reconstruction. This minimized the risk of structural mismatches or artifacts that may occur in cross-species or cross-site applications. The exposure time remained constant at 5-second per projection. 16-bit datasets were reconstructed using Scout and Scan Control System Re-constructor (Carl Zeiss microscopy, Germany). In-situ micro-CT tensile testing was performed using Deben CT500 (Deben, UK) under load control. Tendon-to-bone specimens (l = 20 mm) were mounted in tensile rigs, with the bone (l = 5 mm) clamped at the top jaw and MTJ (l = 5 mm) secured at the bottom jaw, with a 10 mm separation between jaws. This configuration provided a stable environment for the application of the tensile load. Initial micro-CT scans were performed at a nominal preload of 0.2 N. Subsequent to these scans, a non-destructive uniaxial tensile force was applied and increased to reach a load of 4.5 N with 0.1 mm min⁻¹ motor speed and 100 mS sample time, selected based on prior tensile to failure tests and the corresponding force-displacement curve (Supplementary Fig. 12) and held at this value for 15 minutes to allow for tissue viscoelastic relaxation and mechanical stabilization. Initially, we evaluated hold times of 0, 5, 10, and 15 minutes by performing scans at each time point after loading. The scans acquired after 15 minutes were consistently stable, whereas shorter hold times resulted in minor artefacts due to ongoing tissue relaxation. After reaching the maximum load of 4.5 N, the load control was stopped; however, the sample remained under the displacement induced by the 4.5 N loading (average elongation of 1.75 ± 0.1 mm). Due to variation in diameter along the tendon-to-bone specimen, global strain and stress were not calculated; instead, local strain distributions were evaluated using DVC analysis. After the loading stage, samples were re-scanned to capture the load-induced displacement state. No additional loading was applied during the micro-CT scan. The Force Displacement curves were recorded after each test. XRM Data Explorer software was used to convert the datasets from TXM file to BIN as one file.

Image processing and morphometric analysis

The datasets were processed using Avizo software (Thermofischer Scientific, USA). The CFC region was first isolated as a $650 \times 300 \times 300$ voxel volume, where the 650-voxel dimension corresponds to the mediolateral axis. Segmentation was performed using the Magic Wand function to accurately delineate the CFC boundaries. Thickness measurements were then obtained using Avizo's Thickness Map function. This approach computes a voxel-wise thickness by determining, for each voxel, the diameter of the largest sphere that can be fully inscribed within the object. Initially, an Euclidean distance map is generated to assign each voxel a distance value, which is then used to initialize the thickness map. For each voxel, the algorithm examines a spherical neighbourhood (cantered at the voxel and with a radius equal to its distance value) and updates the thickness based on the maximal inscribed sphere, with the final value obtained by doubling the distance to yield the sphere's full diameter. To ensure a consistent visual representation across all samples, colormaps were standardized to a range of 0 to 45. The pre-load and load-induced displacement data were rigidly registered using Avizo software (ThermoFisher Scientific, USA) with a correlation metric and Quasi Newton optimizer to ensure accurate observation of full-field deformation within the CFC. This registration was performed in a semiautomatic manner, where automatic registration was first conducted by the software, and in cases where alignment was insufficient, manual adjustments were made by overlaying the datasets and moving the sample in all three planes to match identifiable anatomical features precisely. The pre-load dataset was used as the reference for resampling the load-induced displacement registered dataset (lattice dimension $650 \times 300 \times 300$). The dataset was then exported as raw 3D data. Morphometric analysis was performed⁵⁹, and is briefly outlined here. Datasets were imported into XamFlow software (Lucid AG, Switzerland). Intensity histograms of pre-load and load-induced displacement tomograms were matched using a micro-CT scan of a hydroxyapatite (HA) phantom (part number 345360-1001-250, Kit 345360-0000-043,

Carl Zeiss Microscopy, USA). Pores were segmented by reverse thresholding, followed by a morphological opening operation to separate connected lacunae for counting and individual labelling. Lacunae volumes were restricted to $50{-}1000\,\mu\text{m}^3$, and morphometric parameters including lacunar oblateness (Lc.Ob) and lacunar stretch (Lc.St) were automatically calculated by XamFlow software. Lc.Ob characterizes the shape from rod-like (-1) to plate-like (+1), while Lc.St describes the shape from a sphere (0) to an infinite plane $(1)^{61}$.

Digital volume correlation uncertainties and analysis

DVC was used to measure the full-field 3D strain at the interface. The reconstructed dataset was imported to DaVis 10.1.5 (LaVision GmbH, Germany) software. For the DVC uncertainties analysis, two consecutive tomograms were acquired in zero strain conditions (Supplementary Note 3, Supplementary Figs. 8 and 9). The uncertainties were estimated using a single step sub volume size 22 (resulted in mean absolute error of less than 1%). Local approach DVC with a multi-step processing scheme was performed using 22 to 52 voxels per sub volume with a 0% overlap, no binning, 1 voxel peak search radius and removed body rigid movement: 8 passes with 22 voxel window size; 4 passes with 32 voxel window size; 4 passes with 42 voxel window size; and 4 passes with 52 voxel window size. Different directional deformations were calculated using vector post processed data of DVC. Maximum normal strain, minimum normal strain, maximum shear strain, and Poisson's ratio were calculated on deformed samples. The strain maps were overlaid on micro-CT datasets in Avizo software, for visualization purposes.

Histology

Histological preparation was carried out 59 , with details summarised here. Specimens were immersed in 10% formalin for 24 h, followed by decalcification in EDTA over a 2-week period. Dehydration was carried out sequentially in 50%, 75%, and 100% ethanol solutions, each for 3 h. Samples were then subjected to xylene clearing (three rounds, 9 hours total), embedded after two cycles of paraffin infiltration (6 h at 60 °C), and finally cast in paraffin wax (Leica, Germany). Sections of 8 μm thickness were obtained using a Leica microtome, mounted on glass slides, heat-fixed at 60 °C for 30 min, and subsequently stained with Hematoxylin (CellPath, UK), Eosin Y (Merck, Germany), and Safranin-O (Merck, Germany). Imaging was performed using a Leica LED digital microscope.

Statistical analysis

Statistical analysis was carried out using GraphPad Prism version 9.4.1 (SD, USA). Data were reported as mean \pm standard deviation, with statistical significance defined at p < 0.05. The Shapiro–Wilk test was applied to assess data normality. Depending on the outcome, either parametric tests (t-test or one-/two-way ANOVA with multiple comparisons) or non-parametric tests were used (n = 3 replicates per group).

Reporting summary

Further information on research design is available in the Nature Portfolio Reporting Summary linked to this article.

Data availability

Representative samples of research data from the experiments and of the data for the figures in the manuscript are provided in the Supplementary Materials. The pre-load and load-induced displacement data are available on Figshare ^{38,39}. The full data is available from the corresponding authors on request.

Received: 12 March 2025; Accepted: 23 September 2025; Published online: 12 November 2025

References

 Genin, G. M. et al. Functional grading of mineral and collagen in the attachment of tendon to bone. *Biophys. J.* 97, 976–985 (2009).

- Wren, T. A. L., Yerby, S. A., Beaupré, G. S. & Carter, D. R. Mechanical properties of the human Achilles tendon. *Clin. Biomech.* 16, 245–251 (2001).
- Thomopoulos, S., Birman, V. & Genin, G. M. Structural linterfaces and Attachments in Biology (Springer Science & Business Media, 2012).
- Rossetti, L. et al. The microstructure and micromechanics of the tendon-bone insertion. *Nat. Mater.* 16, 664–670 (2017).
- Benjamin, M. & Ralphs, J. R. Fibrocartilage in tendons and ligaments
 — an adaptation to compressive load. J. Anat. 193, 481–494 (1998).
- Tits, A. et al. Local anisotropy in mineralized fibrocartilage and subchondral bone beneath the tendon-bone interface. Sci. Rep. 11, 16534 (2021).
- McGonagle, D., Benjamin, M., Marzo-Ortega, H. & Emery, P. Advances in the understanding of entheseal inflammation. *Curr. Rheumatol. Rep.* 4, 500–506 (2002).
- 8. Choi, S. et al. Bone-adhesive anisotropic tough hydrogel mimicking tendon enthesis. *Adv. Mater.* **35**, 2206207 (2023).
- 9. Palastanga, N., Field, D. & Soames, R. *Anatomy and Human Movement: Structure and Function* (Butterworth Heinmann/Elsevier, 2006)
- Benjamin, M. et al. Where tendons and ligaments meet bone: attachment sites ('entheses') in relation to exercise and/or mechanical load. J. Anat. 208, 471–490 (2006).
- Buss, D. J., Rechav, K., Reznikov, N. & McKee, M. D. Mineral tessellation in mouse enthesis fibrocartilage, Achilles tendon, and Hyp calcifying enthesopathy: a shared 3D mineralization pattern. *Bone* 174, 116818 (2023).
- Thomopoulos, S., Genin, G. M. & Galatz, L. M. The development and morphogenesis of the tendon-to-bone insertion What development can teach us about healing. *J. Musculoskelet. Neuronal Interact.* 10, 35 (2010).
- Broom, N. D. & Thambyah, A. The Soft Hard Tissue Junction: Structure, Mechanics and Function (Cambridge University Press, 2018).
- Bregoli, C., Biffi, C. A., Tuissi, A. & Buccino, F. Effect of trabecular architectures on the mechanical response in osteoporotic and healthy human bone. *Med. Biol. Eng. Comput.* 62, 3263–3281 (2024).
- Gao, J. & Messner, K. Quantitative comparison of soft tissue-bone interface at chondral ligament insertions in the rabbit knee joint. *J. Anat.* 188, 367 (1996).
- Goff, E. et al. Large-scale quantification of human osteocyte lacunar morphological biomarkers as assessed by ultra-highresolution desktop micro-computed tomography. *Bone* 152, 116094 (2021).
- 17. Ss, W. The past, present, and future of bone morphometry: its contribution to an improved understanding of bone biology. *J. Bone Miner. Metab.* **23**, 1–10 (2005).
- Fang, J. et al. Decoding the mechanical characteristics of the human anterior cruciate ligament entheses through graduated mineralization interfaces. *Nat. Commun.* 15, 9253 (2024).
- Tits, A. et al. Structural and functional heterogeneity of mineralized fibrocartilage at the Achilles tendon-bone insertion. *Acta Biomater* 166, 409–418 (2023).
- Golman, M. et al. Toughening mechanisms for the attachment of architectured materials: The mechanics of the tendon enthesis. Sci. Adv. 7, eabi5584 (2021).
- Saito, T. et al. The effect of mechanical stress on enthesis homeostasis in a rat Achilles enthesis organ culture model. *J. Orthop.* Res. 40, 1872–1882 (2022).
- Thomopoulos, S., Marquez, J. P., Weinberger, B., Birman, V. & Genin, G. M. Collagen fiber orientation at the tendon to bone insertion and its influence on stress concentrations. *J. Biomech.* 39, 1842–1851 (2006).
- Konofagou, E. E., Spalazzi, J. P. & Lu, H. H. Elastographic imaging of the strain distribution at the anterior cruciate ligament and ACL-bone

- insertions. in 2005 IEEE Engineering in Medicine and Biology 27th Annual Conference 972–975 IEEE, (2006).
- Deymier, A. C. et al. Micro-mechanical properties of the tendon-tobone attachment. Acta Biomater 56, 25–35 (2017).
- 25. Stan, E. et al. A review of histological techniques for differentiating human bone from animal bone. *Methods Protoc.* **7**, 51 (2024).
- Madi, K. et al. In situ characterization of nanoscale strains in loaded whole joints via synchrotron X-ray tomography. *Nat. Biomed. Eng.* 4, 343–354 (2020).
- Vom Scheidt, A., Krug, J., Goggin, P., Bakker, A. D. & Busse, B. 2D vs. 3D evaluation of osteocyte lacunae-methodological approaches, recommended parameters, and challenges: a narrative review by the European Calcified Tissue Society (ECTS). Curr. Osteoporos. Rep. 22, 396–415 (2024).
- Müller, R. Hierarchical microimaging of bone structure and function. Nat. Rev. Rheumatol. 5, 373–381 (2009).
- Du Plessis, A., Broeckhoven, C., Guelpa, A. & Le Roux, S. G. Laboratory x-ray micro-computed tomography: a user guideline for biological samples. *Gigascience* 6, gix027 (2017).
- 30. Maire, E. et al. On the application of x-ray microtomography in the field of materials science. *Adv. Eng. Mater.* **3**, 539–546 (2001).
- Bay, B. K., Smith, T. S., Fyhrie, D. P. & Saad, M. Digital volume correlation: three-dimensional strain mapping using X-ray tomography. *Exp. Mech.* 39, 217–226 (1999).
- Clark, J. N. et al. High resolution three-dimensional strain measurements in human articular cartilage. J. Mech. Behav. Biomed. Mater. 124, 104806 (2021).
- Hussein, A. I., Barbone, P. E. & Morgan, E. F. Digital volume correlation for study of the mechanics of whole bones. *Procedia IUTAM*. 4, 116–125 (2012).
- Villarraga-Gómez, H. et al. Improving scan time and image quality in 3D X-ray microscopy by deep learning reconstruction techniques. in Proc. 35th ASPE Annual Meeting 75, 361–366
- 35. Orhan, K. *Micro-Computed Tomography (micro-CT) in Medicine and Engineering* (Springer, (020).
- Griffin, L. D., Elangovan, P., Mundell, A. & Hezel, D. C. Improved segmentation of meteorite micro-CT images using local histograms. Comput. Geosci. 39, 129–134 (2012).
- 37. Feldkamp, L. A., Davis, L. C. & Kress, J. W. Practical cone-beam algorithm. *Josa A* 1, 612–619 (1984).
- Moayedi, A. Pre-load micro-CT of mouse Achilles to calcaneus interface (calcified fibrocartilage). https://doi.org/10.6084/m9. figshare.28633328.v1 (2025).
- Moayedi, A. Post-load micro-CT of mouse Achilles to calcaneus interface (calcified fibrocartilage). https://doi.org/10.6084/m9. figshare.28633334.v1 (2025).
- Pietsch, P. et al. Quantifying microstructural dynamics and electrochemical activity of graphite and silicon-graphite lithium ion battery anodes. *Nat. Commun.* 7, 12909 (2016).
- 41. Elices, M. Structural Biological Materials: Design and Structure-Property Relationships (Elsevier, 2000).
- Huang, C. & Chen, L. Negative Poisson's ratio in modern functional materials. Adv. Mater. 28, 8079–8096 (2016).
- 43. Gatt, R. et al. Negative Poisson's ratios in tendons: an unexpected mechanical response. *Acta Biomater* **24**, 201–208 (2015).
- Silva, M. J., Brodt, M. D. & Hucker, W. J. Finite element analysis of the mouse tibia: Estimating endocortical strain during three-point bending in SAMP6 osteoporotic mice. *Anat. Rec. Part A Discov. Mol. Cell. Evol. Biol.* 283, 380–390 (2005).
- Said, K. A. M., Jambek, A. B. & Sulaiman, N. A study of image processing using morphological opening and closing processes. *Int. J. Control Theory Appl.* 9, 15–21 (2016).
- Benjamin, M. et al. The skeletal attachment of tendons—tendon 'entheses'. Comp. Biochem. Physiol. Part A Mol. Integr. Physiol. 133, 931–945 (2002).

- Shaw, H. M. & Benjamin, M. Structure–function relationships of entheses in relation to mechanical load and exercise. *Scand. J. Med. Sci. Sports* 17, 303–315 (2007).
- Depalle, B., Qin, Z., Shefelbine, S. J. & Buehler, M. J. Large deformation mechanisms, plasticity, and failure of an individual collagen fibril with different mineral content. *J. Bone Miner. Res.* 31, 380–390 (2016).
- Su, Z. et al. Understanding the mechanics of the temporomandibular joint osteochondral interface from micro-and nanoscopic perspectives. *Nano Lett.* 23, 11702–11709 (2023).
- Sartori, J., Köhring, S., Witte, H., Fischer, M. S. & Löffler, M. Threedimensional imaging of the fibrous microstructure of Achilles tendon entheses in Mus musculus. *J. Anat.* 233, 370–380 (2018).
- Sartori, J., Köhring, S., Bruns, S., Moosmann, J. & Hammel, J. U. Gaining insight into the deformation of Achilles tendon entheses in mice. *Adv. Eng. Mater.* 23, 2100085 (2021).
- Ishimoto, T., Kawahara, K., Matsugaki, A., Kamioka, H. & Nakano, T. Quantitative evaluation of osteocyte morphology and bone anisotropic extracellular matrix in rat femur. *Calcif. Tissue Int.* 109, 434–444 (2021).
- Tits, A. Attaching Soft to Hard: A Multimodal Correlative Investigation of the Tendon-Bone Interface. (2023).
- Kerschnitzki, M. et al. The organization of the osteocyte network mirrors the extracellular matrix orientation in bone. *J. Struct. Biol.* 173, 303–311 (2011).
- Chaumel, J. et al. Co-aligned chondrocytes: zonal morphological variation and structured arrangement of cell lacunae in tessellated cartilage. *Bone* 134, 115264 (2020).
- Buehler, M. J. & Yung, Y. C. Deformation and failure of protein materials in physiologically extreme conditions and disease. *Nat. Mater.* 8, 175–188 (2009).
- Rigozzi, S., Müller, R., Stemmer, A. & Snedeker, J. G. Tendon glycosaminoglycan proteoglycan sidechains promote collagen fibril sliding—AFM observations at the nanoscale. *J. Biomech.* 46, 813–818 (2013).
- Lee, A. H. & Elliott, D. M. Freezing does not alter multiscale tendon mechanics and damage mechanisms in tension. *Ann. N. Y. Acad. Sci.* 1409, 85–94 (2017).
- Moayedi, A. et al. Evaluating the impact of contrast agents on micro and nano mechanics of soft-to-hard tissue interface. Sci. Rep. 15, 28267 (2025).
- Bouxsein, M. L. et al. Guidelines for assessment of bone microstructure in rodents using micro-computed tomography. *J. Bone Miner. Res.* 25, 1468–1486 (2010).
- Coulombe, J. C. et al. Reduced local mechanical stimuli in spaceflight diminishes osteocyte lacunar morphometry and spatial heterogeneity in mouse cortical bone. *bioRxiv* 2001, 2022 (2022).

Acknowledgements

Research was supported by the School of Electrical and Mechanical Engineering at the University of Portsmouth and Carl Zeiss Microscopy, Germany. We acknowledge the support of Dr. Tor Hildebrand and Dr. Peter Suter at Lucid AG, Switzerland, for the support for morphometry analysis; Susan Candell at Carl Zeiss X-ray Microscopy, Dublin, CA, for providing the HA phantom; and Dr. Rosy Manser and Dr. Charles Wood for their support with the Zeiss micro-CT imaging facility and the Deep Recon software license at the Future Technology Centre, University of Portsmouth.

Author contributions

The study was designed by A.M., G.B., and J.R. The resources were provided by G.B., J.R., and M.B.; A.M. developed the methodology and conducted the experiments, supervised by G.B., J.R. M.B., and K.K. Data analyses, visualization, and interpretation were performed by A.M. The manuscript was written by A.M. and reviewed by all authors. The project was administrated by G.B. and J.R.

Competing interests

The authors declare no competing interests.

Additional information

Supplementary information The online version contains supplementary material available at https://doi.org/10.1038/s43246-025-00972-3.

Correspondence and requests for materials should be addressed to Atousa Moayedi.

Peer review information *Communications Materials* thanks Saeed Jerban and the other, anonymous, reviewer(s) for their contribution to the peer review of this work. Primary Handling Editor: John Plummer. A peer review file is available.

Reprints and permissions information is available at http://www.nature.com/reprints

Publisher's note Springer Nature remains neutral with regard to jurisdictional claims in published maps and institutional affiliations.

Open Access This article is licensed under a Creative Commons Attribution 4.0 International License, which permits use, sharing, adaptation, distribution and reproduction in any medium or format, as long as you give appropriate credit to the original author(s) and the source, provide a link to the Creative Commons licence, and indicate if changes were made. The images or other third party material in this article are included in the article's Creative Commons licence, unless indicated otherwise in a credit line to the material. If material is not included in the article's Creative Commons licence and your intended use is not permitted by statutory regulation or exceeds the permitted use, you will need to obtain permission directly from the copyright holder. To view a copy of this licence, visit http://creativecommons.org/licenses/by/4.0/.

© The Author(s) 2025